
Universiteit
Leiden
The Netherlands

The strong phase object approximation may allow extending crystallographic phases of dynamical electron diffraction patterns of 3D protein nano-crystals

Abrahams, J.P.

Citation
Abrahams, J. P. (2010). The strong phase object approximation may allow extending crystallographic phases of dynamical electron diffraction patterns of 3D protein nano-crystals. *Zeitschrift Für Kristallographie*, *225*(2-3), 67-76. doi:10.1524/zkri.2010.1216

Version:	Publisher's Version
License:	Licensed under Article 25fa Copyright Act/Law (Amendment Taverne)
Downloaded from:	https://hdl.handle.net/1887/3621057

Note: To cite this publication please use the final published version (if applicable).

Z. Kristallogr. **225** (2010) 67–76 / **DOI** 10.1524/zkri.2010.1216
© by Oldenbourg Wissenschaftsverlag, München

The strong phase object approximation may allow extending crystallographic phases of dynamical electron diffraction patterns of 3D protein nano-crystals

Jan Pieter Abrahams*

Leiden Institute of Chemistry, Gorlaeus Laboratories, Einsteinweg 55, 2333 CC Leiden, The Netherlands

Received August 3, 2009; accepted November 13, 2009

Phase information / Diffraction patterns / Precession electron diffraction

Abstract. Simulations suggest that the strong phase object approximation of dynamical scattering may allow extracting crystallographic phase information from single 2D electron diffraction patterns of 3D protein crystals using probabilitistic procedures. Unlike other phasing methods, the procedure does not require any additional knowledge – like real space images, atomicity, non-crystallographic symmetry, the presence or location of disordered solvent or the availability of a support with a known structure. In specific cases, the availability of precession electron diffraction data can further improve the phases.

Introduction

When protein crystals fail to grow to a size sufficient for X-ray crystallography, electron diffraction may be a viable alternative (Georgieva *et al*., 2007). The reason why electron diffraction is a more attractive option for very small crystals than X-ray diffraction, is that for each elastically diffracted quantum, electrons on average deposit less energy in the sample than X-rays (Henderson, 1995). However, the issue has been raised that for crystals of proteins that are more than just a few unit cells in thickness, dynamic scattering may prevent structure solution (*e.g.* Glaeser and Downing, 1993).

Dynamical diffraction occurs when electrons scatter elastically more than once in the sample. This effect has been modelled in the multi-slice approach in the Cowley-Moodie formulation of dynamical diffraction theory (Cowley & Moodie, 1957). The regime for dynamical scattering from bacteriorhodopsin 2D crystals was indicated by Glaeser & Ceska (1989): differences between Friedel pairs caused by dynamic scattering were clearly observed when 20 kV electron diffraction patterns were collected; however, they were not observed in 100 kV patterns. For 3D protein crystals, which are considerably thicker than 2D protein crystals, differences between Friedel mates were anticipated even at high accelerating voltage (*e.g.* Glaeser and Downing, 1993)[1] and are indeed also observed experimentally (*e.g.* Jiang *et al*., 2009).

A brief summary of electron diffraction is given here, mainly serving to define some terms that are used throughout the paper. An incoming, coherent electron plane wave passes through a crystalline sample that has a three dimensional scattering potential $V(\vec{x}, z)$, where $\vec{x}$ is a 2D real space vector in the plane of the electron wave and z represents the third dimension in the direction of the beam. The wavelength of the electrons is slightly compressed in areas with a higher potential and an *exit wave* emerges that can be described by a 2D complex *exit wave function* $\psi(\vec{x})$. The *exit wave phase shift* of $\psi(\vec{x})$ is proportional to the projected potential of the sample at the position defined by $\vec{x}$. In photon optics this shifting of the exit wave phases in the absence of absorption, is known as refraction. If absorption occurs, the *exit wave amplitude* $|\psi(\vec{x})|$ is also affected, again proportional to the projected potential of the sample experienced by the electron. Off-axial diffraction occurs, but at high electron energies and moderate resolution, this angular scattering can safely be ignored, leading to the so-called "strong phase object approximation" (Schiff, 1952; Spence, 2003; Glaeser *et al*., 2007), see also Fig. 1. In Appendix I it is shown that the strong phase object approximation is practically equivalent to the multi-slice approach of dynamical electron scattering for high energy electrons at resolutions typical of protein crystals. When off-axial scattering can be ignored, the exit electron plane wave $\psi(\vec{x})$ is therefore determined by the projected potential of the sample ($\varrho_{\perp}(\vec{x}) = \int V(\vec{x}, z)\, \partial z$):

$$\psi(\vec{x}) = c\, \mathrm{e}^{-q\varrho_{\perp}(\vec{x})} \tag{1}$$

In this equation, the factor c is a scale factor proportional to the electron dose. The imaginary term of the exponen-

* e-mail: abrahams@chem.leidenuniv.nl

[1] However, the Friedel pair differences were overestimated in Glaeser and Downing (1993), since their calculations assumed a zero scattering potential for the disordered solvent and lipid parts of the crystal (which on average occupy 50% of the unit cell in protein crystals), resulting in a substantial overestimation of the phase shift of electrons that traveled through ordered protein, compared to electrons that traversed the disordered parts of the crystal.

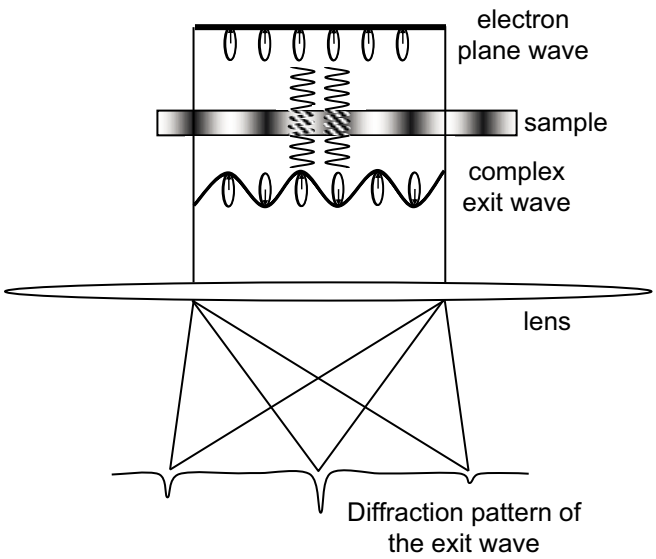

Fig. 1. The strong phase object approximation assumes the wavelength of elastically interacting electrons to be compressed when passing through more electron dense parts of the sample. The shift in phase that results, is proportional to the projected potential of the sample and converts a uniform incoming plane wave into an exit plane wave that has non-uniform phases and no amplitude contrast (if there is no absorption). The lens system of the electron microscope diffracts the exit plane wave into a diffraction pattern in which the Friedel pairs have different intensities if the exit wave is non-centrosymmetric (this asymmetry follows from the mathematical properties of the Fourier transform).

tial complex factor $(q = q_r + iq_i)$ defines the phase shift $\left(q_i = \frac{e^-}{\hbar\nu}\right)$. The real term q_r corrects for absorption and inelastic scattering. Replacing the complex part of the exponential of lemma (1) by its logarithm (the first term of its Taylor expansion), will lead to the weak phase approximation, which assumes single electron scattering (*e.g.* Spence, 2003, Glaeser *et al*., 2009). This is a good approximation, provided the variation in $\varrho_\perp(\vec{x})$ is sufficiently small. In electron diffraction theory, the weak phase approximation is the counterpart of kinematic X-ray diffraction.

In the discussion below, the weak phase approximation is *not* assumed. Instead, the exit wave function defined in lemma (1) is assumed, which results from axial dynamical scattering. Off-axial dynamical scatter is ignored. In this approximation, the dynamic nature of the forward scatter is determined by the projected potential of the sample. Ignoring off-axial scattering and only assuming axial dynamical scattering has led to successful analyses of radiation hard crystalline material using the column approach (*e.g.* Van Dyck and De Beek, 1996), and it is a worthwhile approximation for protein crystals too (see also Appendix I).

Note that although the exit wave function as defined in (1) is complex, at a constant instrument parameter q, it is determined by a single, real valued function: the projected potential $\varrho_\perp(\vec{x})$. As a result, the complex value of the exit wave function $\psi(\vec{x})$ is confined to a logarithmic spiral in the complex plane. The scale of this complex plane spiral is determined by q_i and its pitch is determined by q_r, which are uniform for a given sample and microscope setting. The phasing procedure that is proposed here makes use of this strong constraint that limits the values of $\psi(\vec{x})$. This restraint allows extracting crystallographic phase information from diffraction patterns. Below it is referred to as the 'spiral constraint'.

Especially for crystalline samples, the most extreme contrast is generated in diffraction mode. In diffraction mode, the lens system of the electron microscope does not generate a projection image of the exit wave function, but instead generates a diffraction pattern of $\psi(\vec{x})$ with intensities $I(\vec{h})$ that are discrete if the sample is periodic (Fig. 1). At low scattering angles these intensities are determined by the Fourier transform of $\psi(\vec{x})$, both in the weak and the strong phase object approximation. At higher scattering angles, parallax has to be taken into account, which is essentially described by the curvature of the Ewald sphere. For resolutions up to 2 Å at electron energies between 100 keV to 300 keV (with relativistic electron wavelengths varying between $\lambda_r \approx 0.035$ Å and $\lambda_r \approx 0.015$ Å, respectively), the curvature of the Ewald sphere can be ignored. Resolutions up to 2 Å can be achieved for 3D protein crystals (Georgieva *et al.*, 2007). If we ignore the curvature of the Ewald sphere, the *structure factors* $F(\vec{h})$ of the exit wave function $\psi(\vec{x})$ are defined by a Fourier transform[2]:

$$F(\vec{h}) = \int_{-\infty}^{\infty} \psi(\vec{x})\, \mathrm{e}^{-2i\pi\vec{x}\,\cdot\,\vec{h}}\, \partial\vec{x} = \Im(\psi(\vec{x})) \tag{2}$$

Since the number of data points in $F(\vec{h})$ is limited, the relationship between the structure factors and the parameters describing the electrostatic potential is usually described by the discrete equivalent of (2), summing $\vec{x}$ (in fractional coordinates) over the unit cell and ignoring a constant scale factor N[3]:

$$F(\vec{h_m}) = \sum_n c\, \mathrm{e}^{-q\varrho_\perp(\vec{x_n})}\, \mathrm{e}^{-2i\pi\vec{x_n}\,\cdot\,\vec{h_m}} \tag{4}$$

The diffracted intensities $I(\vec{h_m})$ that are measured by the detector, are determined by the norms of $F(\vec{h_m})$ (note that $\overline{F(\vec{h_m})}$ is the complex conjugate of $F(\vec{h_m})$):

$$I(\vec{h_m}) = F(\vec{h_m})\, \overline{F(\vec{h_m})} \tag{5}$$

Only the intensities can be measured, so reconstruction of the projected potential $\varrho_\perp(\vec{x})$ requires knowledge of the *crystallographic phases* of $F(\vec{h_m})$. In general, it is not possible to infer these crystallographic phases from the measured diffraction data $I(\vec{h_m})$ in the absence of additional knowledge if the Fourier transform of $F(\vec{h_m})$ is a real-valued function. For instance, in the case of kinematic data, where the Fourier transform of $F_{\mathrm{kin}}(\vec{h_m})$ is real-valued, $F_{\mathrm{kin}}(\vec{h_m})$ and $F_{\mathrm{kin}}(-\vec{h_m})$ are *not* independent, but strictly

[2] $\Im(\,)$ signifies the forward Fourier transform.

[3] For kinematic X-ray data, the equivalent relation is:

$$F_{\mathrm{kin}}(\vec{h_m}) = \sum_n c\varrho_\perp(\vec{x_n})\, \mathrm{e}^{-2i\pi\vec{x_n}\cdot\vec{h_m}} \tag{3}$$

Note that in the absence of anomalous effects, this is the discrete Fourier transform of the real-valued real space function $c\varrho_\perp(\vec{x_n})$, whereas (4) is the discrete Fourier transform of the complex-valued real space function $c\,\mathrm{e}^{-q\varrho_\perp(\vec{x_n})}$, which is complex because q is a complex number.

correlated:

$$F_{\mathrm{kin}}(\vec{h_m}) = \sum_n c\varrho_\perp(\vec{x_n})\, \mathrm{e}^{-2\pi i \vec{x_n}\cdot\vec{h_m}} = \overline{F_{\mathrm{kin}}(-\vec{h_m})} \qquad (6)$$

From (5) and (6) Friedel's law can be deduced, which states that the distribution of measured intensities in reciprocal space is centrosymmetric when the real space density is real-valued (or has a uniform phase):

$$I_{\mathrm{kin}}(\vec{h_m}) = I_{\mathrm{kin}}(-\vec{h_m}) \qquad (7)$$

Friedel's law reduces the number of independent equations as expressed in (5) to $\frac{N}{2}$ (one for each positive $\vec{h_m}$), but there are still N independent real-valued electrostatic potential parameters (all $\varrho_\perp(\vec{x})$). This dashes all hopes for a solution of the crystallographic phases in the absence of additional knowledge in the case of kinematic diffraction. Crystallographic symmetry reduces the number of independent (unknown) density parameters. However, this symmetry is maintained when switching from real to reciprocal space, so it also reduces by an equal amount the number measured independent data points and independent equations. However, other types of knowledge can successfully reduce the number of independent parameters and hence allow phasing. Additional information like atomicity (at high resolution), non-crystallographic symmetry, solvent flatness and (local) structural similarities will most certainly help in specific cases, but are by no means universal and may not apply to single diffraction images (which correspond to projections of structures). Hence these additional types of information cannot be part of a general solution of the phase problem.

However, for dynamical electron diffraction the problem appears to be more tractable than for kinematic diffraction. In order to understand this, one has to consider that for dynamical scattering, the number of independent measurements defined by (5) *does* equal the number of independent unknown electrostatic potential parameters (all $\varrho_\perp(\vec{x})$). Briefly, in the case of dynamic scattering, if there are N independent real-valued measurements, corresponding to N equations (all $I(\vec{h_m})$), then there are also N independent real-valued projected electrostatic potential parameters (all $\varrho_\perp(\vec{x})$). The reason is that, in contrast to kinematical diffraction, Friedel's law does *not* apply to dynamical electron diffraction, as inspection of (4) reveals: the Fourier terms of (4) have an imaginary component, which is not the case in kinematical approximations. For dynamical diffraction, the number of independent measurements expressed in (5) therefore *does* match the number of unknown parameters, kindling the hope for a solution to the phase problem in the case of dynamical diffraction. Attempts (some more successful than others) have been made to use this knowledge for *ab initio* determination of small molecule structures (*e.g.* Spence *et al.*, 1999 and references therein), but so far no practical applications have emerged.

If the terms summed in (5) would be linear and independent, there would be a unique solution, even for structures as large as protein crystals. Although the equations are independent, they are not linear, so there might be multiple solutions. In general, solving such a set of non-linear equations is not straightforward and the usual strategy involves iteratively improving reasonable starting values. Here, a maximum likelihood approach including a conjugate gradient minimization is discussed, that reconstructs phase information from a (very) poor initial estimate.

Methods

Minimization

Several strategies can be envisaged to extract phase information from (5). In the absence of additional information, all these strategies, in one way or another, aim to solve the set of non-linear equations that result upon substituting (4) into (5). As a first exploration, a probabilistic approach is followed here. Assuming a Gaussian error model, minimizing χ^2 will identify the most probable solutions of the phases[4]:

$$\chi^2 = \sum_m \frac{(I_o(\vec{h_m}) - I(\vec{h_m}))^2}{\sigma^2(\vec{h_m})} \qquad (8)$$

The number of free parameters (exit wave phase shifts defined by $\varrho_\perp(\vec{x})$ in (4) equals the number of summations in (8) if just a single diffraction pattern is observed, so there are no degrees of freedom. If 3D diffraction data are collected, the number of degrees of freedom becomes more favourable. A positive number of degrees of freedom allows calculating the probability of the model of the electrostatic potential, given the measured diffraction data and its (inferred) variance, and using an incomplete gamma function. However, full 3D data collection is not considered in this study, but the benefit of limited 3D data collection through precessing the sample *is* investigated (see below). The partial derivatives of χ^2 to the projected density $\varrho_\perp(\vec{x})$ are given by[5]:

$$\frac{\partial\chi^2}{\partial\varrho_\perp(\vec{x_n})} = 4c\left[\overline{q}\,\mathrm{e}^{-\overline{q}\varrho_\perp(\vec{x_n})}\,\Im^{-1}\left(F(\vec{h_m})\frac{I_o(\vec{h_m}) - I(\vec{h_m})}{\sigma^2(\vec{h_m})}\right)\right]_{\mathrm{real}} \qquad (9)$$

These partial derivatives define the gradient of χ^2. This gradient can be conditioned in orthogonal directions by dividing it by the second partial derivatives. This curvature is approximated by[6]:

$$\frac{\partial^2\chi^2}{\partial\varrho_\perp^2(\vec{x})} \approx 4c^2 q\overline{q}\,\mathrm{e}^{-(q+\overline{q})\,\varrho_\perp(\vec{x_n})}\sum_m \frac{I(\vec{h_m})}{\sigma^2(\vec{h_m})} \qquad (10)$$

Dividing (9) by (10) results in the Newton step $N_s(\vec{x})$:

$$N_s(\vec{x}) = \left[\frac{\Im^{-1}\left(F(\vec{h_m})\frac{I_o(\vec{h_m}) - I(\vec{h_m})}{\sigma^2(\vec{h_m})}\right)}{cq\,\mathrm{e}^{-q\varrho_\perp(\vec{x_n})}\sum_m \frac{I(\vec{h_m})}{\sigma^2(\vec{h_m})}}\right]_{\mathrm{real}} \qquad (11)$$

[4] $I_o(\vec{h_m})$ is the observed intensity with standard deviation $\sigma(\vec{h_m})$.

[5] $\Im()^{-1}$ signifies the inverse Fourier transform, $\bar{q}$ is the complex conjugate of q; for a proof of lemma (9) see Appendix II.

[6] For a proof of lemma (10), see Appendix III.

If this Newton step is subtracted from any estimate of $\varrho_\perp(\vec{x})$, it would minimize χ^2 in a single iteration if (8) was truly quadratic and if there were no correlations between its terms. Even though this is not the case, taking Newton steps down the multidimensional gradient is a logical approach towards minimizing χ^2. Although it would be feasible to specifically introduce the correlations between the terms of (8) by also considering off-diagonal terms in (10), the matrix operations would quickly become unwieldy for larger problems. Another reason for ignoring off-diagonal terms is that the Hessian is diagonally dominant (see Appendix III). Instead, correlations can be taken into account by adopting a variant of the Polak–Ribière conjugate gradient minimisation algorithm. At iteration p of the minimization procedure, the corresponding Newton step $N_{s,p}(\vec{x_p})$ can be calculated and the target χ^2 function explored in a direction $d_p(\vec{x})$ that is essentially orthogonal to directions explored in earlier iterations[7]:

$$d_p(\vec{x_n}) = \beta d_{p-1}(\vec{x_n}) - N_{s,p}(\vec{x_n}) \tag{12}$$

Improved density at iteration p was calculated using the following equation, where the magnitude of α is iteratively reduced by half (starting from unity) until χ^2 is smaller than in the previous iteration[8]:

$$\varrho_{\perp,p}(\vec{x_n}) = \varrho_{\perp,p-1}(\vec{x_n}) + \alpha d_p(\vec{x_n}) \tag{13}$$

The procedures outlined above were implemented in C++, using the FFTW3 library (Frigo & Johnson, 2005) for calculating the Fourier transforms.

Simulating electron precession data

It has been documented that precessing the beam during the electron diffraction experiment, reduces the observed dynamic scattering (Vincent & Midgley 1994). It was therefore investigated whether it is beneficial to include electron precession data as additional constraints in the optimization procedure outlined above. Testing this hypothesis required modelling the effect of electron precession on dynamic electron diffraction patterns. Precession was simulated by calculating diffraction patterns of the sample, each tilted by a fixed angle κ about an axis within the plane of $\psi(\vec{x})$. The direction of the tilt axis within the plane of $\psi(\vec{x})$ is defined by ω. Since the sample is periodic in the z-direction, tilting the crystal by a small angle will result in slightly misaligning the projections of the stacked unit cells in the direction normal to the tilt axis, which results in a smearing of the projected electrostatic potential in this direction. At larger tilt angles (or at higher resolution), other periodicities of the crystal would come into view, corresponding to the next Laue zones in the reciprocal lattice. In these cases, knowledge of the full 3D structure is required to calculate the projected potential. This was not what was simulated, however. Instead, a small angle tilt of a the 3D crystal was simulated by smearing the projected density in the direction of the tilt by convoluting the exit wave-function with an anisotropic 2D Gaussian function $B_\omega(\vec{x})$ defined by[9]:

$$B_\omega(\vec{x_n}) = \exp\left(-\left(\vec{x_n}\begin{pmatrix}\cos\omega & \sin\omega\\ -\sin\omega & \cos\omega\end{pmatrix}\cdot\vec{b}\right)^2\right) \tag{14}$$

Rather than calculating the full convolution, the Fourier convolution theorem was applied in order to generate the projected potential of the tilted sample:

$$\varrho_{\perp,\omega}(\vec{x_n}) = \Im^{-1}(\Im(\varrho_{\perp,\omega}(\vec{x_n}))\,\Im(B_\omega(\vec{x_n}))) \tag{15}$$

After simulating the effect of tilting the crystalline sample on the projected potential, the exit wave $\psi_\omega(\vec{x_n})$ of the tilted crystal was calculated using lemma (4), replacing $\varrho_\perp(\vec{x_n})$ by the tilted potential $\varrho_{\perp,\omega}(\vec{x_n})$. The corresponding structure factors were simulated by calculating the Fourier transform according to lemma (4), using $\psi_\omega(\vec{x_n})$ as input. This result was then used to calculate the tilted crystallographic diffraction intensities $I_\omega(\vec{h_m})$ using lemma (5).

In this study the effect of separately collecting a set of diffraction patterns, each obtained at a different in-plane rotation axis ω was investigated, rather than collecting a single diffraction pattern, fully integrated over ω. In practice this type of data collection has very recently been realized for radiation hard crystals (S. Hovmöller, *pers. comm.*). With fast, low-noise detectors and by slowing down the precession rate, this is also within the current technical capabilities for protein crystals. Using a set of diffraction patterns, rather than a single diffraction pattern, marginally complicates the minimization algorithm outlined above. Essentially, χ^2 is accumulated over all angles ω at which diffraction patterns were collected[10]:

$$\chi^2 = \sum_\omega \sum_m \frac{(I_{o,\omega}(\vec{h_m}) - I_\omega(\vec{h_m}))^2}{\sigma^2_\omega(\vec{h_m})} \tag{16}$$

Minimizing (16) requires the Newton steps to be accumulated over all angles ω.

Generating test data

The strong phase object approximation only considers the projected electron scattering potential of the sample, not on the distribution of its potential in z. Hence, only a sin-

[7] In the Polak-Ribière variant of conjugate gradient minimisation, the scalar β is calculated from previous gradient information:

$$\beta = \max\left(0, \frac{N_{s,p}(\vec{x})\cdot(N_{s,p}(\vec{x}) - N_{s,p-1}(\vec{x}))}{N_{s,p-1}(\vec{x})\cdot N_{s,p-1}(\vec{x})}\right)$$

In the Fletcher-Reeves variant, the scalar β is given by:

$$\beta = \frac{N_{s,p}(\vec{x})\cdot N_{s,p}(\vec{x})}{N_{s,p-1}(\vec{x})\cdot N_{s,p-1}(\vec{x})}$$

For steepest descent minimisation, $\beta = 0$.

[8] Note that this implies that there are no elaborate (time consuming) line minimisations in the search direction. As a side effect, it turned out that there is not much difference in performance between steepest descent, Polak-Ribière and Fletcher-Reeves algorithms for overall minimisation, the latter two being marginally faster, but also having a marginally increased tendency to stop prematurely.

[9] In this equation, the vector $\vec{b}$ defines the width of the Gaussian in the directions along and normal to the axis defined by ω. For all tests reported in here, $\vec{b} = \{0; 0.2\}$, expressed in pixels.

[10] $I_{o,\omega}(\vec{h_n})$ and $\sigma^2_\omega(\vec{h_m})$ are the observed intensities and intensity variances of the diffraction pattern collected at an in-plane rotation axis ω.

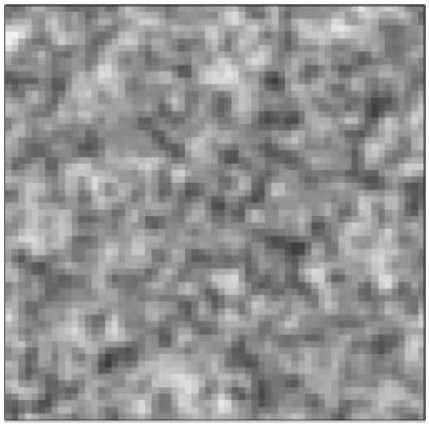

Fig. 2. A simulated projection of a single unit cell in *P*1 with a random structure. The minimum density is 9 arbitrary units, the maximum density is 10 arbitrary units.

gle 2D projection of the scattering potential needs to be considered when evaluating restrictions on the reciprocal space phases of a single diffraction pattern that are imposed by the strong phase approximation.

Random, discrete 2D images of projected electron scattering potential of various sizes and using various random number seeds were generated and tested. Here only the results of projection images with a size of 64 by 64 data points are discussed, but for smaller and larger sizes similar results were obtained. Each data point of the image was assigned a random electron scattering potential between 9 and 10 (arbitrary units). The images were marginally smoothed with an exponential decay filter, to simulate the high resolution correlations that are present in protein density due to its secondary structure, and which, for instance, contribute to the well known Wilson distribution of protein diffraction data. No other restraints, like crystallographic or non-crystallographic symmetry, solvent flatness, atomicity, expected histograms or support- or windowing functions were imposed on the projection images. A typical example is shown in Fig. 2 and this simulated density was used for all the tests reported here. Using other simulated densities with similar statistics led to similar conclusions. Initial guesses were generated from the true structure by filtering it with another, much stronger and more selective exponential decay function[11]:

$$\varrho_i(\vec{x_n}) = \Im^{-1}\left(\Im(\varrho_\perp(\vec{x_n}))\exp\left(-\frac{|\vec{h_m}|}{|\vec{h}|_{\max}}b_i\right)\right) \qquad (17)$$

For those reciprocal points in which the exponent in (17) was smaller than a specified cut-off value, this exponent was set to zero. This allowed completely discarding part of the phase information from the initial guess in a resolution dependent manner. For all tests reported here, 5000 cycles of minimization were performed, taking approximately 10 milliseconds per cycle on a normal desktop computer. For the tests reported, the parameters defining the relation between $\psi(\vec{x})$ and $\varrho_\perp(\vec{x})$ defined in lemma (1) were set to $(c = 1)$, $(q_r = 0.01)$ and either $(q_i = 2\pi)$ for full phase scrambling or $\left(q_i = \frac{\pi}{6}\right)$ for simulating less extreme dynamic scattering. For evaluating the results, correlation coefficients between the true projection structure and test projection structures were calculated after having optimized the translational alignment between the true structure and the test structure.

[11] $|\vec{h_m}|$ is the length of $\vec{h_m}$ in reciprocal pixels; $|\vec{h}|_{\max}$ is the maximum length of $\vec{h}$ in reciprocal pixels ($32\sqrt{2}$ in the tests reported here, as a unit cell of 64 by 64 pixels is assumed); b_i is a constant that was changed for generating different starting models.

Results

The spiral constraint minimization procedure outlined above, iteratively improves an initial estimate of the phases. It was therefore tested how poor such an initial estimate can be, yet still allow phase extension. Many tests were performed in order to identify the limits of the spiral constraint and a consistent picture emerges that is illustrated here with some examples. Included in these tests were various values for q_i, including zero, in order to test whether absorption effects had any significant influence on the results. This did not appear to be the case.

Most of the tests described here assumed a complete phase scrambling: the pixels with the highest potential in $\varrho_\perp(\vec{x_n})$ would then result in a 2π phase shift in $\psi(\vec{x_n})$, relative to the pixels with the lowest potential. In protein crystals this is a worst case scenario, as it results in a complete lack of correlation between Friedel pairs. This is not what is typically observed in diffraction patterns of 3D protein nano-crystals (*e.g.* Georgieva *et al.*, 2009). Tests with less extreme dynamic scattering tended to give better results.

For single diffraction patterns, the spiral constraint allows the crystallographic phases to be reconstructed moderately well. An initial guess (shown in Fig. 3a) in which almost half of the crystallographic phase information had been discarded, can be improved to a projection image that essentially captures the high resolution details of the true structure (Fig. 3b), provided the phases are not fully scrambled. If the phases are fully scrambled, the result is somewhat poorer (Fig. 3c). More impressive results are obtained when using precession data (Fig. 4). A very poor initial guess, only containing information from a 3% remnant of all the low resolution crystallographic phases (Fig. 4a) could be improved to a projected density that is indistinguishable from the true structure (Fig. 4d). In this particular case, 40 separate diffraction patterns were fed into the spiral constraint routine, each the result of tilting about a different axis in the plane of the projection image. Figure 4b and 4c show examples of the real space projected potential, from which two of these diffraction patterns were calculated. If only a single, non-tilted diffraction pattern is used, the result bears only little resemblance to the true projection structure, indicating that precession data enhances the phasing procedure outlined above (Fig. 4e).

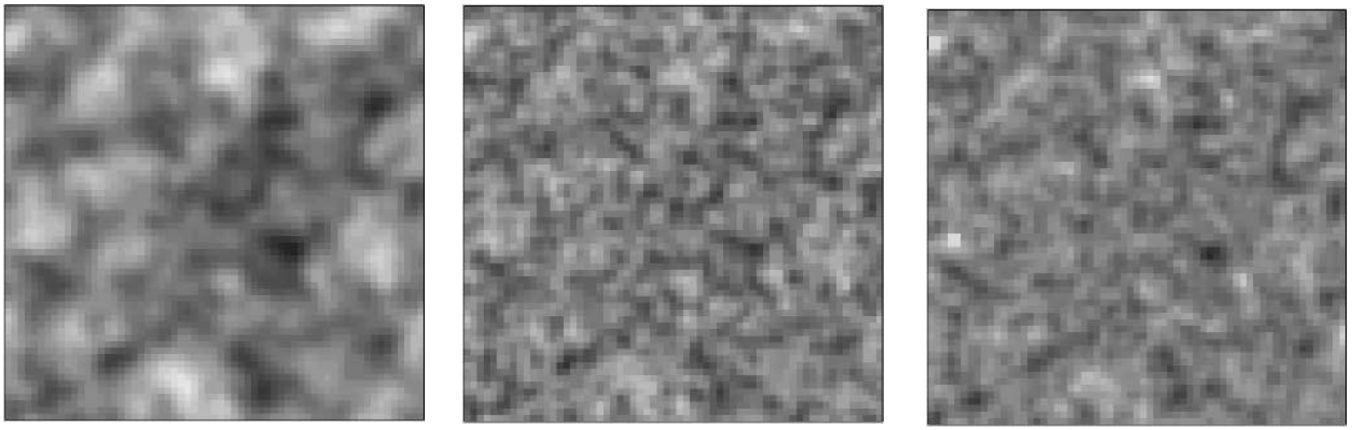

Fig. 3. (**a**) An initial estimate of the projection structure for refinement against a single diffraction pattern, obtained by setting b_i to -20 and using a cut-off for the exponential of 10^{-5} in (17), resulting in 2129 non-zero structure factors (from a total of 4096). This initial estimate has a correlation coefficient of 0.16 with the true projection structure and a starting χ^2 of 10^5 $\left(\text{for } q = \left(0.01; \frac{\pi}{6}\right)\right)$ or 2.9×10^7 (for $q = (0.01; 2\pi)$). (**b**) Projection structure after 5000 rounds of refinement against diffraction data calculated using (5), after setting $q = \left(0.01; \frac{\pi}{6}\right)$ and $c = 1$ in (4). This results in a maximum phase difference in the exit wave of $\frac{\pi}{6}$. The correlation coefficient with the true projection structure is 0.076, with a χ^2 of 4.3. The result indicates the projection structure can be reconstructed well. (**c**) Result after 5000 rounds of minimisation, but this time setting $q = (0.01; 2\pi)$, resulting in complete phase scrambling and a much stronger simulated dynamical scattering effect. The correlation coefficient with the true projection structure is 0.14, with a χ^2 of 2550, indicating poor reconstruction of the phases.

Discussion

The results indicate that the spiral constraint is a promising option for attempting to phase dynamical electron diffraction data, especially in the case of protein diffraction data. Such data do not tend to extend to high resolution, whilst also the unit cell is so large that the restraint of atomicity cannot be imposed, since the potential of so many atoms partially overlap in projection. Initial tests suggest that inclusion of electron precession data substantially enhance the procedure, when the diffraction frames at different tilt angles are collected separately. Currently this mode of data collection has not been thoroughly explored, but there are no technical limitations that would prevent such a data collection strategy.

Phase improvement could also have been implemented in a Gerchberg–Saxton type algorithm (Gerchberg & Saxton, 1972), as in Fourier cycling (*e.g.* phase extension by solvent flattening (Wang, 1985)), or flipping procedures for reducing model bias (Abrahams, 1997; Oszlanyi & Suto, 2004). Such implementation would entail alternately imposing constraints in real space[12] and the crystallographic structure factor amplitude constraints in reciprocal space, whilst switching between real and reciprocal space by forward and reverse Fourier transforms. The Fourier cycling approach does not allow the satisfactory inclusion of the (inferred) standard deviations that are due to counting statistics or other sources of variability. For including such information, the χ^2 statistic as expressed in (8) is a much more attractive minimisation target. Assuming the Central Limit Theorem, the χ^2 statistic even allows estimating the probability of the outcome, using χ^2 and the degrees of freedom as inputs to an incomplete gamma-function. Nevertheless, a Fourier cycling algorithm was also evaluated in view of its almost trivial implementation. It turned out not to be very successful, most likely because it cycles between two unconstrained complex functions, whereas lemma (1) indicates that the complex function in the real space domain has a very special shape, being confined to running along a logarithmic spiral – as pointed out in the introduction. The spiral constraint imposes that the real space function runs along this spiral track, substantially reducing its scope. Indeed, it is precisely this constraint of $\psi(\vec{x})$ as a highly restricted function in the complex domain that allows extracting phase information in the first place!

If the illuminating beam is structured and especially if its structure results in sharp features in the real space projection image, knowledge of its precise shape can be used for phasing (*e.g.* Guizar–Sicairos & Fienup, 2008; Martin & Allen, 2008). The procedure outlined here does not require such additional information, though the presence of such information might enhance its success rate.

There are many other sources of additional information that can be included in the outlined procedure. These include solvent flatness, histogram information (*e.g.* Zhang & Main, 1990), atomicity (at high resolution), non-crystallographic symmetry, heavy atom information, molecular replacement solutions. Perhaps most relevant in the case of electron diffraction is to include image information (*e.g.* Henderson & Unwin, 1975; Weirich *et al.*, 1996), which allows phasing of the low resolution crystallographic structure factors. The spiral constraint method outlined here, might then be used to extend these phases.

[12] Such constraints would minimally include the absence of amplitude contrast, or a strict correlation between the phase and the amplitude contrast as defined in (8).

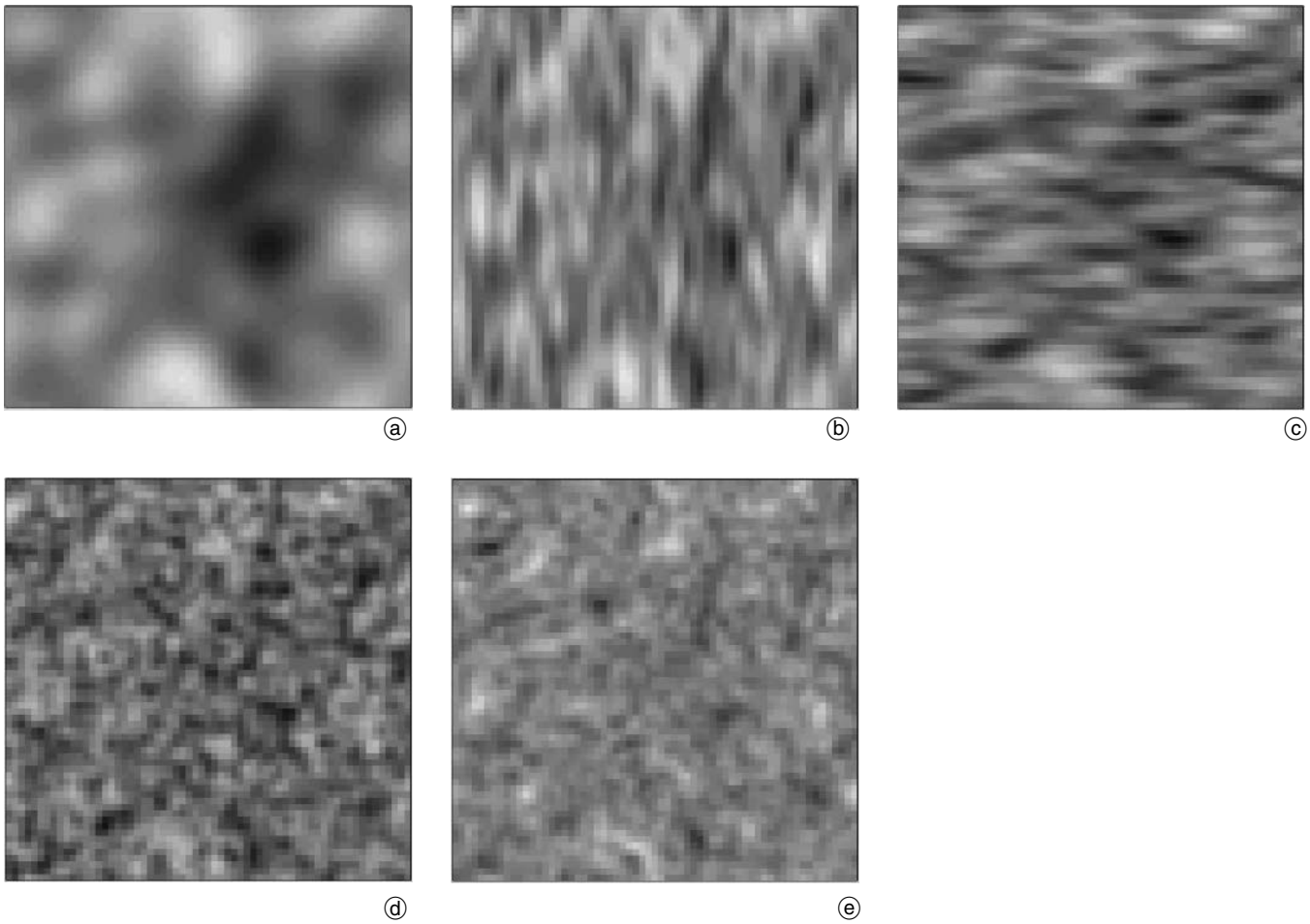

Fig. 4. An initial estimate of the projection structure for refinement against 40 diffraction patterns from a precession series, obtained by setting b_i to -20 and using a cut-off for the exponential of 0.06 in (17), resulting in 129 non-zero structure factors (from a total of 4096). This initial estimate has a correlation coefficient of 0.161 with the true projection structure and a starting χ^2 of 10^9 against the 40 diffraction patterns. (**b**) and (**c**) show two examples of projected potentials corresponding to two diffraction patterns from the precession series. The angles of the tilt axes are 0 and $\frac{\pi}{2}$, respectively. The tilt angle corresponding to these projection simulations would be defined by the thickness of the crystal and the coherence length of the electrons. Within reasonable limits, this can be estimated to be about 0.14 radians for the densities shown, which is well within the experimental capabilities of current equipment. (**d**) Result after 5000 rounds of minimisation against all 40 patterns from the precession series, setting $q = (0.01; 2\pi)$, resulting in complete phase scrambling. The correlation coefficient with the true projection structure is 0.003 with a χ^2 of 2.3, indicating excellent, full reconstruction of the phases. (**e**) Result after 5000 rounds of minimisation starting with the guess depicted in (**a**) against a single, non-tilted diffraction pattern, whilst setting $q = (0.01; 2\pi)$. The correlation coefficient with the true projection structure is 0.205 with a χ^2 of 3.7×10^3, indicating failure to reconstruct phases.

If it becomes possible to collect full 3D electron diffraction data sets of single protein nano-crystals, additional sources of crystallographic phase information can be tapped. This would be the ultimate expansion of minimising (16), and the assumption of a small precession angle should be abandoned. In this case $I_\omega(\vec{h_m})$ would have to be calculated differently, assuming the full 3D density[13]:

$$I_\Omega(\vec{h_m}) = \Im(c \exp(-q \int V((\vec{x}, z)\, \Omega)\, \partial z))$$

The advantage of such 3D diffraction data is that substantially more mutually independent data can be gathered than in the 2D approach. This should allow phasing the crystallographic structure factors using the spiral constraint from very poor initial estimates and might even allow *ab initio* phasing.

[13] Rather than a single rotation *angle* ω defining the tilt axis of crystalline sample as in (16), a rotation *matrix* Ω would be required to calculate all possible diffraction patterns.

Appendix I: The strong phase object approximation as a special case of the multislice approach to dynamic scattering

In the multislice simulation of dynamical high-energy electron scattering, the sample is computationally divided into thin slices (with thickness Δz) that are orthogonal to the direction of the electron beam. At each slice, the electron wave function experiences a local phase shift due to the potential through which it travels. The slices are thin enough to allow this phase shift to be calculated from the projected atomic potential according to lemma (1); within a slice, no lateral diffractive spreading of the electron wave function is assumed. After the electron beam has passed though a slice, Fresnel diffraction is assumed as the beam travels onward towards the next slice. This Fresnel diffraction is simulated by convoluting the electron wave function that exits the slice, with the Fresnel propagator function. The phases of this modified electron wave function are then shifted according to the projected den-

sity of the next slice, followed by another convolution with the Fresnel propagator function. The procedure is repeated until the electron wave has passed through all the slices of the sample.

Following the notation in (Kirkland, 1998), this can be formulated as a recursive function[14]:

$$\psi(\vec{x}, z + \Delta z) = p(\vec{x}, \Delta z) \otimes [t(\vec{x}, z)\ \psi(\vec{x}, z)] \tag{18}$$

The recursive function starts with $\psi(\vec{x}, 0)$ being a plane wave. The transmission functions $t(\vec{x}, z)$ of the recursive multislice equation are defined analogously to (1) as:

$$t(\vec{x}, z) = c \exp\left(-q\varrho_{\Delta z}(\vec{x}, z)\right) \tag{19}$$

The projected potential $\varrho_{\Delta z}(\vec{x}, z)$ is integrated between the planes at the slice boundaries:

$$\varrho_{\Delta z}(\vec{x}, z) = \int_{z}^{z+\Delta z} V(\vec{x}, z)\, \partial z \tag{20}$$

The Fresnel propagator $p(\vec{x}, \Delta z)$ that determines the off-axial diffraction is defined as:

$$p(\vec{x}, \Delta z) = -\frac{i}{\lambda\, \Delta z} \exp\left(i\pi \frac{|\vec{x}|^2}{\lambda\, \Delta z}\right) \tag{21}$$

At given microscope settings, the Fresnel propagator $p(\vec{x}, \Delta z)$ is a complex function with a constant modulus or amplitude: $|p(\vec{x}, \Delta z)| = (\lambda\, \Delta z)^{-1}$. It is rotationally symmetrical, is purely complex at the origin and its argument (phase) varies with $|x|^2$, the squared distance from the origin.

In practice, the convolutions of the recursive multislice function (18) are calculated assuming a discrete real space potential function $\varrho_{\Delta z}(\vec{x}, z)$, requiring the Fresnel propagator (or its Fourier transform) to also be turned into a discrete function. The mathematical properties of this propagator function dictate that this discretization needs to be done with great care. At larger distances from the origin, the argument of $p(\vec{x}, \Delta z)$ is highly critically dependent on the variable $|x|^2$, and can go through many cycles between adjacent spatial sampling intervals. In this light, it would clearly be a bad idea to use sampling for calculating the value of $p(\vec{x}, \Delta z)$ at discrete points using lemma (21). Far from the origin, even a shift in the spatial parameter that is much smaller than the experimental accuracy or computational significance, would result in a completely different argument of $p(\vec{x}, \Delta z)$, which would lead to unpredictable results. Instead it is much better to discretize $p(\vec{x}, \Delta z)$ by locally integrating this function around the discrete spatial sampling points.

At what spatial resolutions is this local average of $p(\vec{x}, \Delta z)$ no longer significant for the convolution? The integrals are not analytical, but a good estimate of the extent of the locally smeared $p(\vec{x}, \Delta z)$ can be made. At $\left(\frac{|\vec{x}|^2}{\lambda\, \Delta z} = 2\right)$, the Fresnel propagator will have gone fully round the complex circle, compared to its value at the origin. Clearly, this sampling of $p(\vec{x}, \Delta z)$ is already far too course. At 100 kV ($\lambda \approx 0.035$ Å) and a slice thickness Δz of 2 Å (corresponding to a typical resolution of protein crystals), the Fresnel propagator will already have made a full revolution at ($\sqrt{2 \cdot 0.035.2} = 0.37$ Å). This is significantly smaller than a spatial sampling interval justified by the typical resolution of protein crystals.

We can conclude that if we sample the potential of a typical protein crystal at spatial intervals that are warranted by its resolution, both in x and y (the plane of the slice) and in the direction of the beam, the dampened Fresnel propagator (which must be used for the multislice calculations), is practically zero everywhere, except at the origin, where it is $(\lambda\, \Delta z)^{-1}$. This being the case, the convolutions of (18) become trivial multiplications with a constant, reducing the multislice equation to the strong phase object approximation given by lemma (1).

Appendix II: Proof of Eq. (9)

First it is assumed that all the density parameters defined by $\varrho_{\perp}(\vec{x_n})$ are uncorrelated over $\vec{x}$, which implies:

$$\frac{\partial \varrho_{\perp}(\vec{x_n})}{\partial \varrho_{\perp}(\vec{x_i})} = 0 \quad \forall i \neq n$$

This independency is an extreme assumption, being a worst-case for minimisation. However, it does allow an important simplification when calculating $\frac{\partial F(\vec{h_m})}{\partial \varrho_{\perp}(\vec{x_n})}$ and $\frac{\partial \overline{F(\vec{h_m})}}{\partial \varrho_{\perp}(\vec{x_n})}$ from (4):

$$\begin{aligned}\frac{\partial F(\vec{h_m})}{\partial \varrho_{\perp}(\vec{x_n})} &= \sum_n \frac{\partial (c\, \mathrm{e}^{-q\varrho_{\perp}(\vec{x_n})})}{\partial \varrho_{\perp}(\vec{x_n})}\, \mathrm{e}^{-2\pi i \vec{x_n} \cdot \vec{h_m}} \\ &= -qc\, \mathrm{e}^{-q\varrho_{\perp}(\vec{x_n})}\, \mathrm{e}^{-2\pi i \vec{x_n} \cdot \vec{h_m}} \end{aligned} \tag{22}$$

$$\frac{\partial \overline{F(\vec{h_m})}}{\partial \varrho_{\perp}(\vec{x_n})} = -\overline{q} c\, \mathrm{e}^{-\overline{q}\varrho_{\perp}(\vec{x_n})}\, \mathrm{e}^{2\pi i \vec{x_n} \cdot \vec{h_m}} = \overline{\left(\frac{\partial F(\vec{h_m})}{\partial \varrho_{\perp}(\vec{x_n})}\right)} \tag{23}$$

These equations are substituted into $\frac{\partial I(\vec{h_m})}{\partial \varrho_{\perp}(\vec{x_n})}$, which results after by applying the product rule to (5):

$$\begin{aligned}\frac{\partial I(\vec{h_m})}{\partial \varrho_{\perp}(\vec{x_i})} &= \frac{\partial F(\vec{h_m})}{\partial \varrho_{\perp}(\vec{x_n})}\, \overline{F(\vec{h_m})} + \frac{\partial \overline{F(\vec{h_m})}}{\partial \varrho_{\perp}(\vec{x_n})}\, F(\vec{h_m}) \\ &= 2 \left[\overline{\left(\frac{\partial F(\vec{h_m})}{\partial \varrho_{\perp}(\vec{x_n})}\right)}\, F(\vec{h_m})\right]_{\text{real}} \\ &= -2c[\overline{q}\, \mathrm{e}^{-\overline{q}\varrho_{\perp}(\vec{x_n})}\, \mathrm{e}^{2\pi i \vec{x_n} \cdot \vec{h_m}}\, F(\vec{h_m})]_{\text{real}} \end{aligned} \tag{24}$$

Applying the chain rule to (8) results in:

$$\frac{\partial \chi^2}{\partial \varrho_{\perp}(\vec{x_n})} = 2 \sum_m \frac{\partial I(\vec{h_m})}{\partial \varrho_{\perp}(\vec{x_n})}\, \frac{I_o(\vec{h_m}) - I(\vec{h_m})}{\sigma^2(\vec{h_m})} \tag{25}$$

[14] The symbol '$\otimes$' is the convolution operator. The multislice equation shown here, omits an additive truncation error term that results from combining the strong phase approximation with the propagator function and that is a function of $\Delta z^2\, \varrho_s(\vec{x}, z)$.

Substituting (24) into (25) results in:

$$\begin{aligned}
&\frac{\partial\chi^2}{\partial\varrho_\perp(\vec{x_n})}\\
&= 4c\sum_m \left[\overline{q}\,\mathrm{e}^{-\overline{q}\varrho_\perp(\vec{x_n})}\,\mathrm{e}^{2\pi i\vec{x_n}\cdot\vec{h_m}}\,F(\vec{h_m})\right]_{\mathrm{real}}\frac{I_o(\vec{h_m})-I(\vec{h_m})}{\sigma^2(\vec{h_m})}\\
&= 4c\left[\overline{q}\,\mathrm{e}^{-\overline{q}\varrho_\perp(\vec{x_n})}\sum_m F(\vec{h_m})\,\frac{I_o(\vec{h_m})-I(\vec{h_m})}{\sigma^2(\vec{h_m})}\,\mathrm{e}^{2\pi i\vec{x_n}\cdot\vec{h_m}}\right]_{\mathrm{real}}
\end{aligned}$$

Appendix III: proof of Eq. (10)

The second derivates of (25) are:

$$\begin{aligned}
\frac{\partial\chi^2}{\partial\varrho_\perp(\vec{x_i})\,\partial\varrho_\perp(\vec{x_j})} &= 2\sum_m \frac{\partial I(\vec{h_m})}{\partial\varrho_\perp(\vec{x_i})}\frac{\partial I(\vec{h_m})}{\partial\varrho_\perp(\vec{x_j})}\,\frac{1}{\sigma^2(\vec{h_m})}\\
&\quad + 2\sum_m \frac{\partial^2 I(\vec{h_m})}{\partial\varrho_\perp^2(\vec{x_n})}\frac{I_o(\vec{h_m})-I(\vec{h_m})}{\sigma^2(\vec{h_m})}
\end{aligned}\tag{26}$$

The second summation term can safely be ignored if we assume $I_o(\vec{h_m})$ and $I(\vec{h_m})$ to be uncorrelated, since in this case the summation $\sum_m (I_o(\vec{h_m})-I(\vec{h_m}))$ will cancel to zero. Substituting with (24) gives:

$$\begin{aligned}
&\frac{\partial\chi^2}{\partial\varrho_\perp(\vec{x_i})\partial\varrho_\perp(\vec{x_j})} \approx 2\sum_m \frac{\partial I(\vec{h_m})}{\partial\varrho_\perp(\vec{x_i})}\frac{\partial I(\vec{h_m})}{\partial\varrho_\perp(\vec{x_j})}\,\frac{1}{\sigma^2(\vec{h_m})}\\
&\approx 2\sum_m \left(q\,\mathrm{e}^{-q\varrho_\perp(\vec{x_i})}\,\overline{F(\vec{h_m})}\,\mathrm{e}^{-2\pi i\vec{x_i}\cdot\vec{h_m}}\right.\\
&\quad \left.+\,\overline{q}\,\mathrm{e}^{-\overline{q}\varrho_\perp(\vec{x_i})}\,F(\vec{h_m})\,\mathrm{e}^{2\pi i\vec{x_i}\cdot\vec{h_m}}\right)\\
&\quad \times\left(q\,\mathrm{e}^{-q\varrho_\perp(\vec{x_j})}\,\overline{F(\vec{h_m})}\,\mathrm{e}^{-2\pi i\vec{x_j}\cdot\vec{h_m}}\right.\\
&\qquad \left.+\,\overline{q}\,\mathrm{e}^{-\overline{q}\varrho_\perp(\vec{x_j})}\,F(\vec{h_m})\,\mathrm{e}^{2\pi i\vec{x_j}\cdot\vec{h_m}}\right)\,\frac{1}{\sigma^2(\vec{h_m})}\\
&\approx 2q^2c^2\sum_m \mathrm{e}^{-q(\varrho_\perp(\vec{x_i})+\varrho_\perp(\vec{x_j}))}\,\frac{\overline{F(\vec{h_m})}^2}{\sigma^2(\vec{h_m})}\,\mathrm{e}^{-2\pi i(\vec{x_i}+\vec{x_j})\cdot\vec{h_m}}\\
&\quad + 2q\overline{q}c^2\sum_m \mathrm{e}^{-q\varrho_\perp(\vec{x_i})-\overline{q}\varrho_\perp(\vec{x_j})}\,\frac{I(\vec{h_m})^2}{\sigma^2(\vec{h_m})}\,\mathrm{e}^{-2\pi i(\vec{x_i}-\vec{x_j})\cdot\vec{h_m}}\\
&\quad + 2q\overline{q}c^2\sum_m \mathrm{e}^{-\overline{q}\varrho_\perp(\vec{x_i})-q\varrho_\perp(\vec{x_j})}\,\frac{I(\vec{h_m})^2}{\sigma^2(\vec{h_m})}\,\mathrm{e}^{-2\pi i(\vec{x_i}-\vec{x_j})\cdot\vec{h_m}}\\
&\quad + 2\overline{q}^2c^2\sum_m \mathrm{e}^{-\overline{q}(\varrho_\perp(\vec{x_i})+\varrho_\perp(\vec{x_j}))}\,\frac{F(\vec{h_m})^2}{\sigma^2(\vec{h_m})}\,\mathrm{e}^{-2\pi i(\vec{x_i}+\vec{x_j})\cdot\vec{h_m}}
\end{aligned}\tag{27}$$

All of the four summations are additions of complex numbers. Assuming that these complex numbers are uncorrelated, that counting statistics apply (in which case $I(\vec{h_m})=\sigma^2(\vec{h_m})$ and $|F^2(\vec{h_m})|=\sigma^2(\vec{h_m})$) and that absorption is negligible ($q_r=0$), the central limit theorem implies that the expected value of each of these summations will be $2q\overline{q}c^2\sqrt{N}$, where N is the number of terms in the summation. There is an exception, however, when $\vec{x_i}=\vec{x_j}$. In this case, the second and third terms of (27) are summations of positive real numbers. These diagonal elements of the Hessian are:

$$\begin{aligned}
\frac{\partial\chi^2}{\partial\varrho_\perp^2(\vec{x_i})} &\approx 4c^2\sum_m q\overline{q}\,\mathrm{e}^{-(\overline{q}+q)\varrho_\perp(\vec{x_i})}\,\frac{I(\vec{h_m})^2}{\sigma^2(\vec{h_m})}\\
&\quad + 4c^2\sum_m\left[\overline{q}^2\,\mathrm{e}^{-2\overline{q}\varrho_\perp(\vec{x_i})}\,\frac{F(\vec{h_m})^2}{\sigma^2(\vec{h_m})}\,\mathrm{e}^{4\pi i\vec{x_i}\cdot\vec{h_m}}\right]_{\mathrm{real}}
\end{aligned}\tag{28}$$

In this case, the expected value of the diagonal terms of the Hessian is $4q\overline{q}c^2(N+\sqrt{N})$. Since N is large, the following approximation of the second partial derivatives is therefore good enough for conditioning the gradient of χ^2:

$$\frac{\partial\chi^2}{\partial\varrho_\perp^2(\vec{x_i})} \approx 4c^2q\overline{q}\,\mathrm{e}^{-(\overline{q}+q)\,\varrho_\perp(\vec{x_i})}\sum_m\frac{I(\vec{h_m})^2}{\sigma^2(\vec{h_m})}$$

Acknowledgments. I sincerely thank RAG de Graaff for carefully reading parts of this manuscript. I also thank Raj Pannu, Pavol Skubak, Irakli Sikharulidze, Linhua Jiang and Dilyana Georgieva for helping me to formulate the ideas expressed here. Any remaining errors are my own. I apologise to my students for not having marked their work as quickly as they had a right to, because I was to busy writing this paper.

References

Abrahams, J. P.: Bias reduction in phase refinement by modified interference functions: Introducing the gamma correction. Acta Cryst. D**53** (1997) 371–376.

Cowley, J.M.; Moodie, A.F.: The scattering of electrons by atoms and crystals (1) a new theoretical approach. Acta Crystallogr. **10** (1957) 609–619.

Frigo, M.; Johnson, S.G.: Design and implementation of FFTW3. Proc. IEEE **93** (2005) 216–231.

Georgieva, D.G.; Kuil, M.E.; Oosterkamp, T.H.; Zandbergen, H.W.; Abrahams, J.P.: Heterogeneous crystallization of protein nanocrystals. Acta Crystallogr. D**63** (2007) 564–570

Gerchberg, R.W.; Saxton, W.O.: A practical algorithm for the determination of the phase from image and diffraction plane pictures. Optik **35** (1972) 237–246.

Glaeser, R.M.; Ceska, T.A.: High-Voltage electron diffraction from bacteriorhodopsin (purple membrane) is measurably dynamical. Acta Crystallogr. A**45** (1989) 620–628.

Glaeser, R.M.; Downing, K.H.: High resolution electron crystallography of protein molecules. Ultramicroscopy **52** (1993) 478–486.

Glaeser, R.M.; Downing, K.; DeRosier, D.; Chiu, W.; Frank, J.: Electron Crystallography of Biological Macromolecules. Oxford Univ. Press. (2007) 416–419.

Guizar-Sicairos, M.; Fienup, J.R.: Direct image reconstruction from a Fourier intensity pattern using HERALDO. Optics Lett. **33** (2008) 2668–2670.

Henderson, R.; Unwin, P.N.T.: Three-dimensional model of the purple membrane obtained by electron microscopy. Nature **257** (1975) 28–32.

Henderson, R.: The potential and limitations of neutrons, electrons and X-rays for atomic resolution microscopy of unstained biological molecules. Quart. Rev. Biophys. **28** (1995) 171–193.

Jiang, L.; Georgieva, D.; Zandbergen H.W.; Abrahams J.P.: Unit-cell determination from randomly oriented electron-diffraction patterns. Acta Crystallogr. D**65** (2009) 625–632.

Kirkland, E.J.: Advanced computing in electron microscopy. Plenum Press. (1998) 106–111.

Martin, A.V.; Allen L.J.: Direct retrieval of a complex wave from its diffraction pattern. Optics Comm. **281** (2008) 5114–5121.

Oszlanyi G.; Suto A.: Ab initio structure solution by charge flipping. Acta Crystallogr. A**60** (2004) 134–141.

Schiff, L.I.: Approximation method for high-energy potential scattering. Phys. Rev. **103(2)** (1956) 443–453.

Spence, J.C.H.; Calef, B; Zou, J.M.: Dynamic Inversion by the method of generalized projections. Acta Crystallogr. A**55** (1999) 112–118.

Spence, J.C.H.: High-Resolution Electron Microscopy. Oxford University Press. (2003) 61–63.

Vincent, R.; Midgley, P.A.: Double conical beamrocking system for measurement of integrated electron diffraction intensities. Ultramicroscopy **53** (1994) 271–281.

Van Dyck, D.; De Beek, M.O.: A simple intuitive theory for electron diffraction. Ultramicroscopy **64** (1996) 99–107.

Wang. B.C.: Resolution of Phase Ambiguity in Macromolecular Crystallography. In: *Diffraction Methods for Biological Macromolecules*. Vol. B115 of Methods in Enzymology. Academic Press, (1985) 90–112.

Weirich, T.E.; Ramlau, R.; Simon, A.; Hovmöller, S.; Zou X.D.: A crystal structure determined with 0.02 angstrom accuracy by electron microscopy. Nature **382** (1996) 144–146.

Zhang, K.Y.J.; Main, P.: The use of Sayre's equation with solvent flattening and histogram matching for phase extension and refinement of protein structures. Acta Crystallogr. A**46** (1990) 377–381.